Electronic Supplementary Material (ESI) for Dalton Transactions.
This journal is © The Royal Society of Chemistry 2020

Homo- and Heteroleptic trimethoxy terpyridine-Cu(II) complexes: Synthesis, Characterization, DNA/BSA Binding, DNA Cleavage and Cytotoxicity Studies

Surbhi Jain[a], Kishalay Bhar[a], Sandeep Kumar[b], Shreetama Bandyopadhyaya[c], Suman Tapryal[b], Chandi C. Mandal[c], Anuj K. Sharma[a]*

[a]*Department of Chemistry, School of Chemical Sciences and Pharmacy, Central University of Rajasthan, Bandarsindri, District Ajmer, Rajasthan, 305817, India.*

[b]*Department of Biotechnology, School of Chemical Sciences and Pharmacy, Central University of Rajasthan, Bandarsindri, District Ajmer, Rajasthan, 305817, India.*

[c]*Department of Biochemistry, School of Chemical Sciences and Pharmacy, Central University of Rajasthan, Bandarsindri, District Ajmer, Rajasthan, 305817, India.*

Supporting Information

Contents

1.	**Figure S1.**	Data and graph for elemental analysis of **C-I**.
2.	**Figure S2.**	Data and graph for elemental analysis of **C-II**.
3.	**Figure S3.**	Data and graph for elemental analysis of **C-III**.
4.	**Figure S4.**	Data and graph for elemental analysis of **C-IV**.
5.	**Figure S5.**	FTIR spectrum of **C-I.**
6.	**Figure S6.**	FTIR spectrum of **C-II.**
7.	**Figure S7.**	FTIR spectrum of **C-III.**
8.	**Figure S8.**	FTIR spectrum of **C-IV.**
9.	**Figure S9.**	^{1}H NMR spectrum of **L** in $CDCl_3$.
10.	**Figure S10.**	^{13}C NMR spectrum of ligand **L** in $CDCl_3$.
11.	**Figure S11**.	ESI-Mass spectrum of **C-I** recorded in MeCN.
12.	**Figure S12**.	ESI-Mass spectrum of **C-II** recorded in MeCN.
13.	**Figure S13**.	ESI-Mass spectrum of **C-III** recorded in MeCN.
14.	**Figure S14.**	UV-vis absorption spectra of **L** in MeCN.
15.	**Figure S15.**	UV- Visible absorption spectra of **C-I** recorded in MeCN and MeCN:PBS buffer (1:1) upto 48 h at 298 K.
16.	**Figure S16.**	UV- Visible absorption spectra of **C-II** recorded in MeCN and MeCN:PBS buffer (1:1) upto 48 h at 298 K.
17.	**Figure S17.**	UV- Visible absorption spectra of **C-III** recorded in MeCN and MeCN:PBS buffer (1:1) upto 48 h at 298 K.
18.	**Figure S18.**	UV- Visible absorption spectra of **C-IV** recorded in MeCN and MeCN:PBS buffer (1:1) upto 48 h at 298 K.
19.	**Figure S19.**	Crystal packing of **C-I** showing π-π interaction and H-bonding.
20.	**Figure S20.**	Crystal packing of **C-II** showing H-bonding.
21.	**Figure S21.**	Crystal packing of **C-IV** showing π-π interaction and H-bonding.
22.	**Figure S22.**	X-band EPR spectrum of complex **C-II** in MeCN glass at 77 K (frequency 9.1 GHz and 100 kHz field).
23.	**Figure S23.**	X-band EPR spectrum of complex **C-III** in MeCN glass at 77 K (frequency 9.1 GHz and 100 kHz field).
24.	**Figure S24.**	X-band EPR spectrum of complex **C-IV** in MeCN glass at 77 K (frequency 9.1 GHz and 100 kHz field).
22.	**Figure S25.**	Cyclic voltammogram of **C-I** (1 mM) solution in dry CH_3CN and 0.1 M TBAP as supporting electrolyte *vs.* Ag wire at varying scan rates.

23.	**Figure S26.**	Cyclic voltammogram of **C-II** (1 mM) solution in dry CH_3CN and 0.1 M TBAP as supporting electrolyte *vs.* Ag wire at varying scan rates.
24.	**Figure S27.**	Cyclic voltammogram of **C-III** (1 mM) solution in dry CH_3CN and 0.1 M TBAP as supporting electrolyte *vs.* Ag wire at varying scan rates.
25.	**Figure S28.**	Cyclic voltammogram of **C-IV** (1 mM) solution in dry CH_3CN and 0.1 M TBAP as supporting electrolyte *vs.* Ag wire at varying scan rates.
26.	**Figure S29.**	Plot of fluorescence emission intensity *I* versus wavelength λ for DNA-EtBr at different concentrations of **C-II**. The arrow shows the change in intensity of emission on increasing amount of the complex from 0 to 50 μM.
27.	**Figure S30.**	Plot of fluorescence emission intensity *I* versus wavelength λ for DNA-EtBr at different concentrations of **C-III**. The arrow shows the change in intensity of emission on increasing amount of the complex from 0 to 50 μM.
28.	**Figure S31.**	Plot of fluorescence emission intensity *I* versus wavelength λ for DNA-EtBr at different concentrations of **C-IV**. The arrow shows the change in intensity of emission on increasing amount of the complex from 0 to 50 μM.
29.	**Figure S32.**	Plot of fluorescence emission intensity *I* versus wavelength λ for BSA at different concentrations of **C-II**. The arrow shows the change in intensity of emission on increasing amount of the complex from 0 to around 50 μM.
30.	**Figure S33.**	Plot of fluorescence emission intensity *I* versus wavelength λ for BSA at different concentrations of **C-III**. The arrow shows the change in intensity of emission on increasing amount of the complex from 0 to around 50 μM.
31.	**Figure S34.**	Plot of fluorescence emission intensity *I* versus wavelength λ for BSA at different concentrations of **C-IV**. The arrow shows the change in intensity of emission on increasing amount of the complex from 0 to around 50 μM.
32.	**Figure S35.**	Agarose gel electrophoresis for complexes **C-I** to **C-IV** showing DNA aggregation in presence of H_2O_2.
33.	**Figure S36.**	Agarose gel electrophoresis for terpyridine ligand and co-ligands in presence of 3-MPA.
34.	**Figure S37.**	
35.	**Table S1.**	Consolidated characterization data for copper(II) complexes (**C-I - C-IV**)
36.	**Table S2.**	Summary of crystal data for complexes **C-I**, **C-II** and **C-IV**
37.	**Table S3.**	Selected bond lengths (Å) and bond angles (°) for complexes **C-I**, **C-II** and **C-IV**
38.	**Table S4.**	Summary of IC_{50} values for similar Cu(II) complexes in cancer cell line.

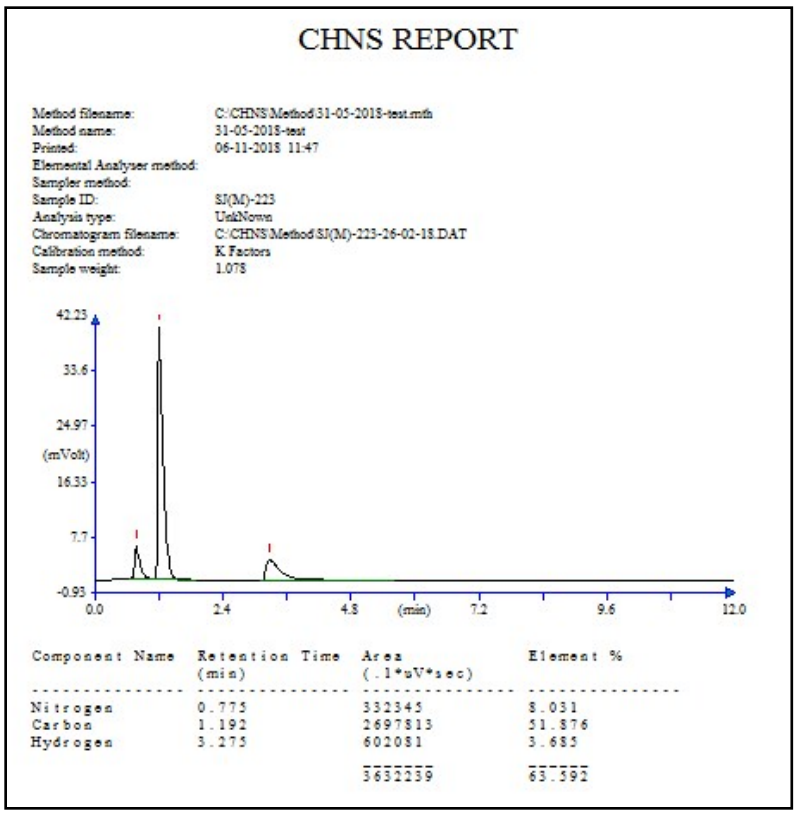

Figure S1. Data and graph for elemental analysis of **C-I**.

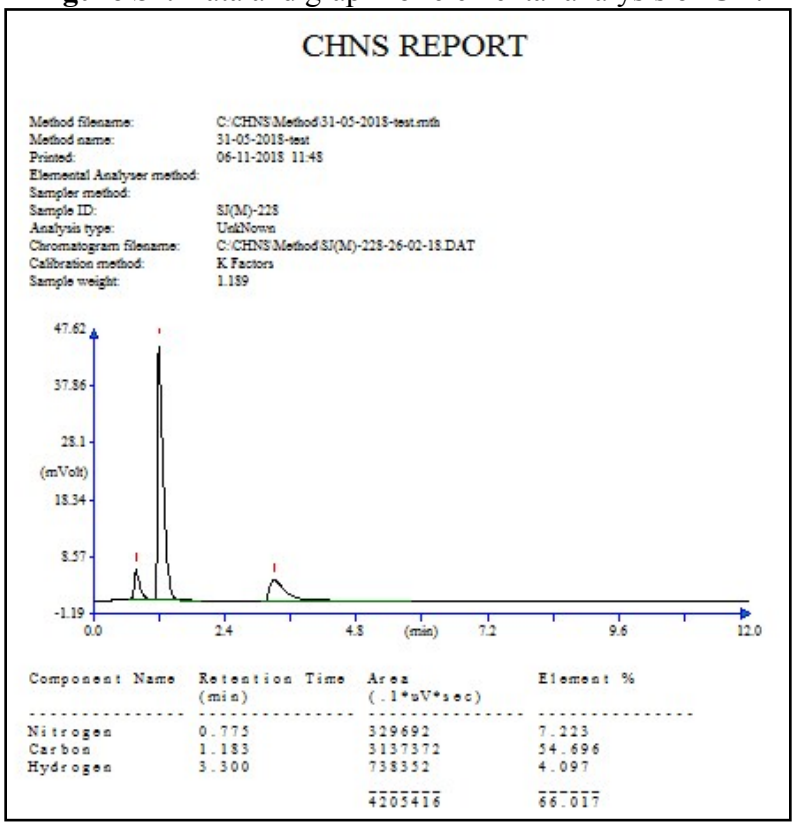

Figure S2. Data and graph for elemental analysis of **C-II**.

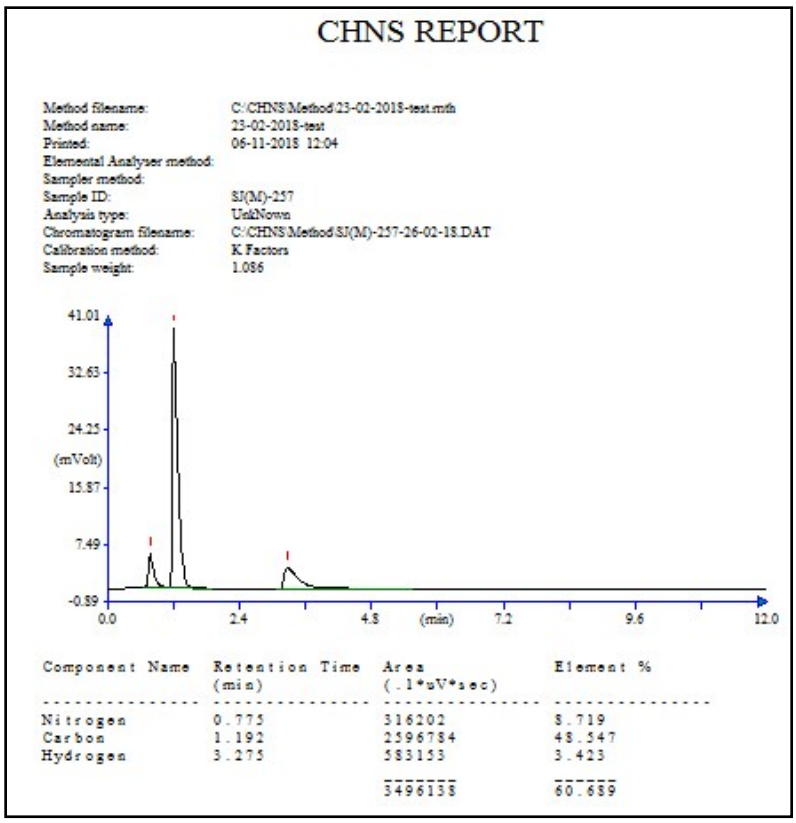

Figure S3. Data and graph for elemental analysis of **C-III**.

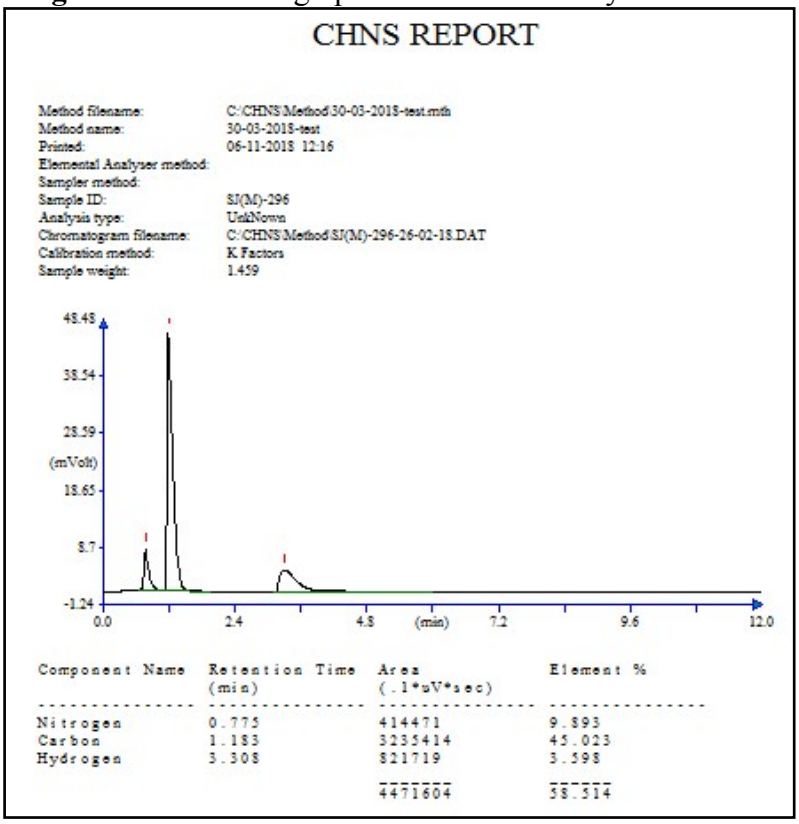

Figure S4. Data and graph for elemental analysis of **C-IV**

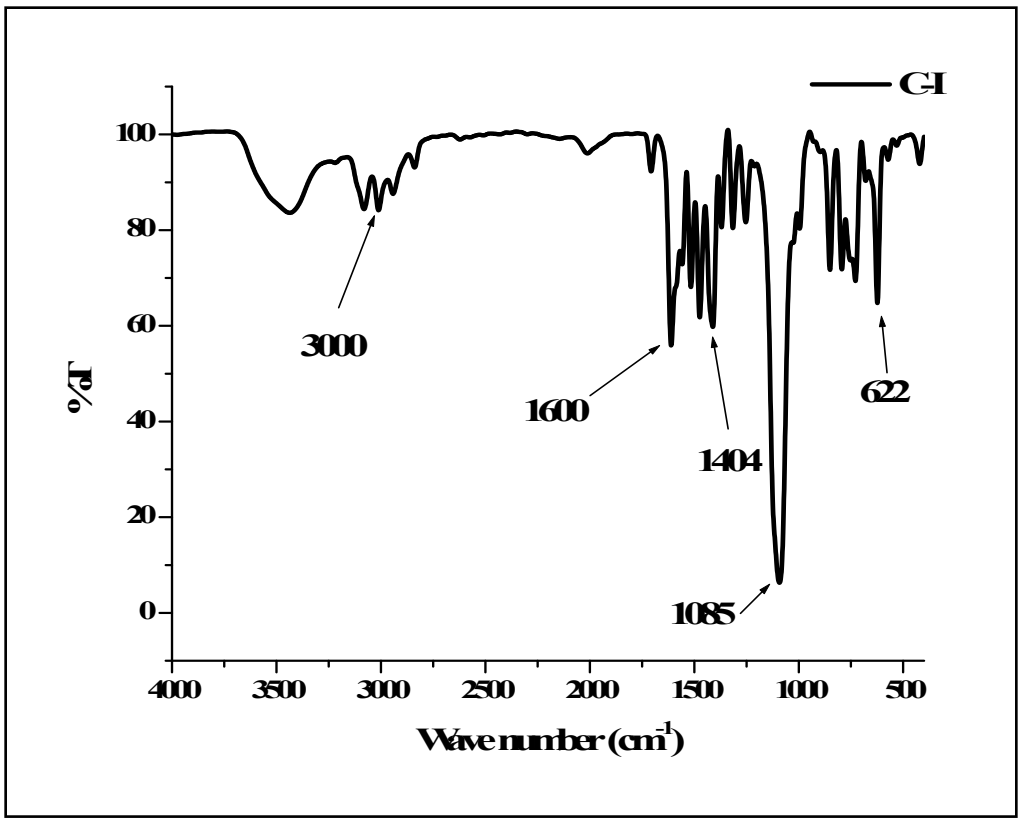

Figure S5. IR spectrum of **C-I**.

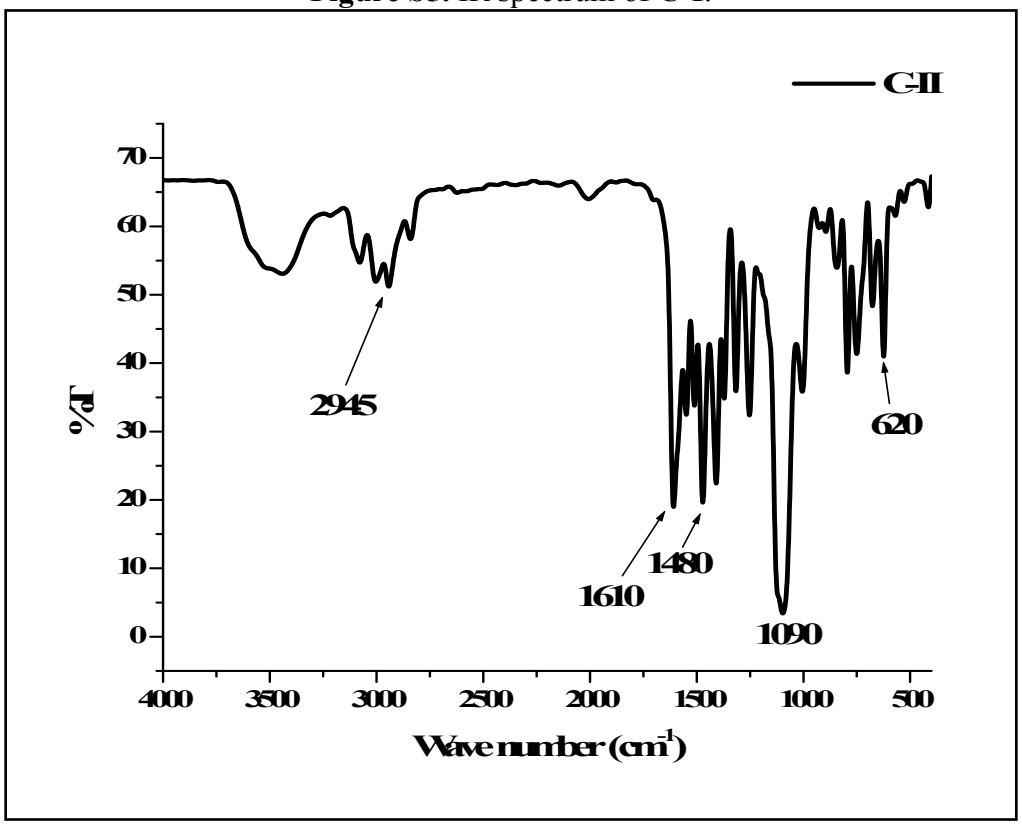

Figure S6. IR spectrum of **C-II**.

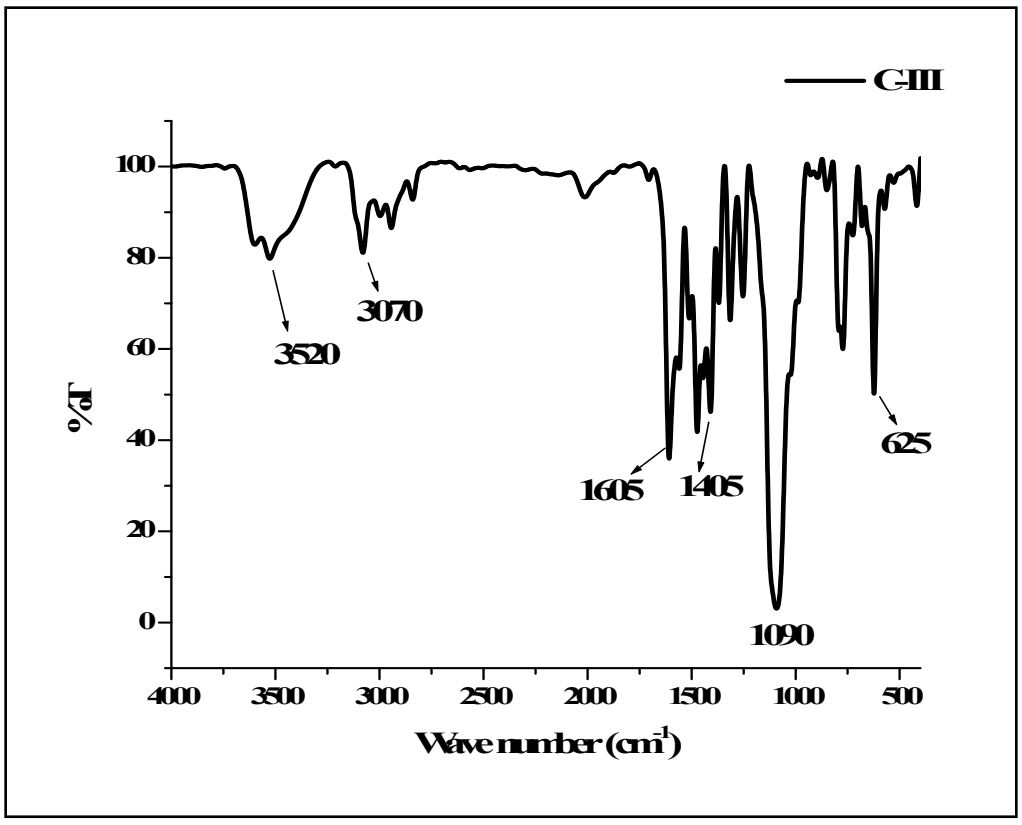

Figure S7. IR spectrum of **C-III**.

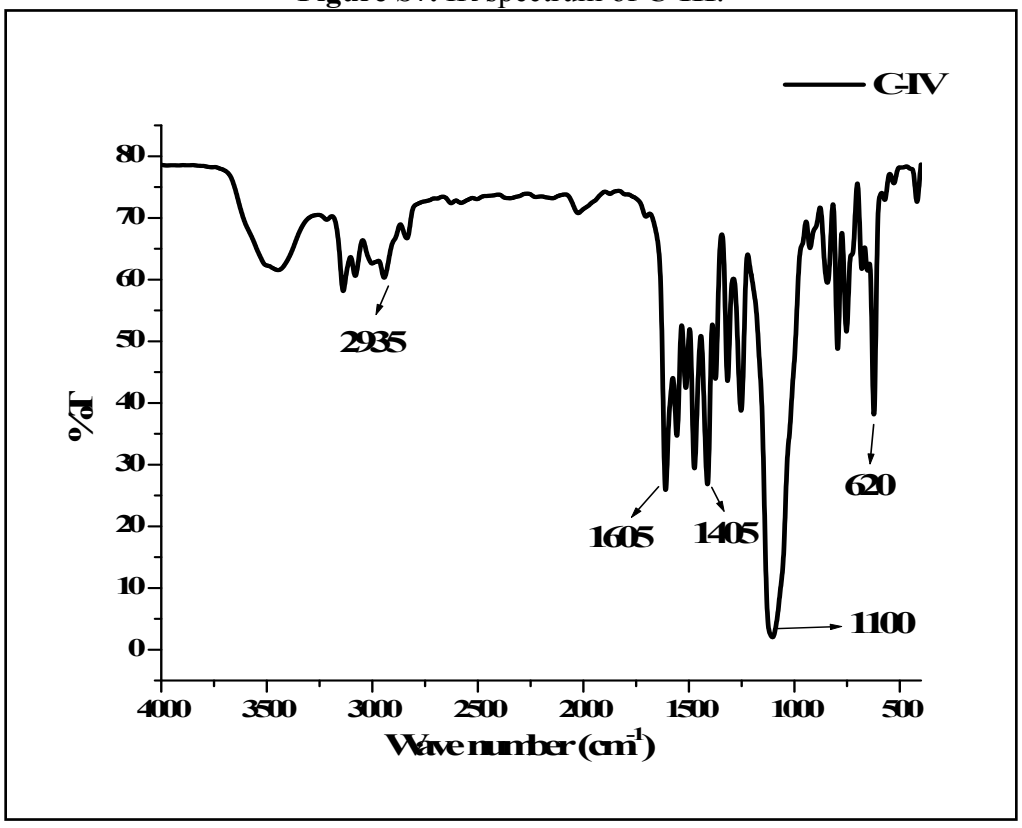

Figure S8. IR spectrum of **C-IV**.

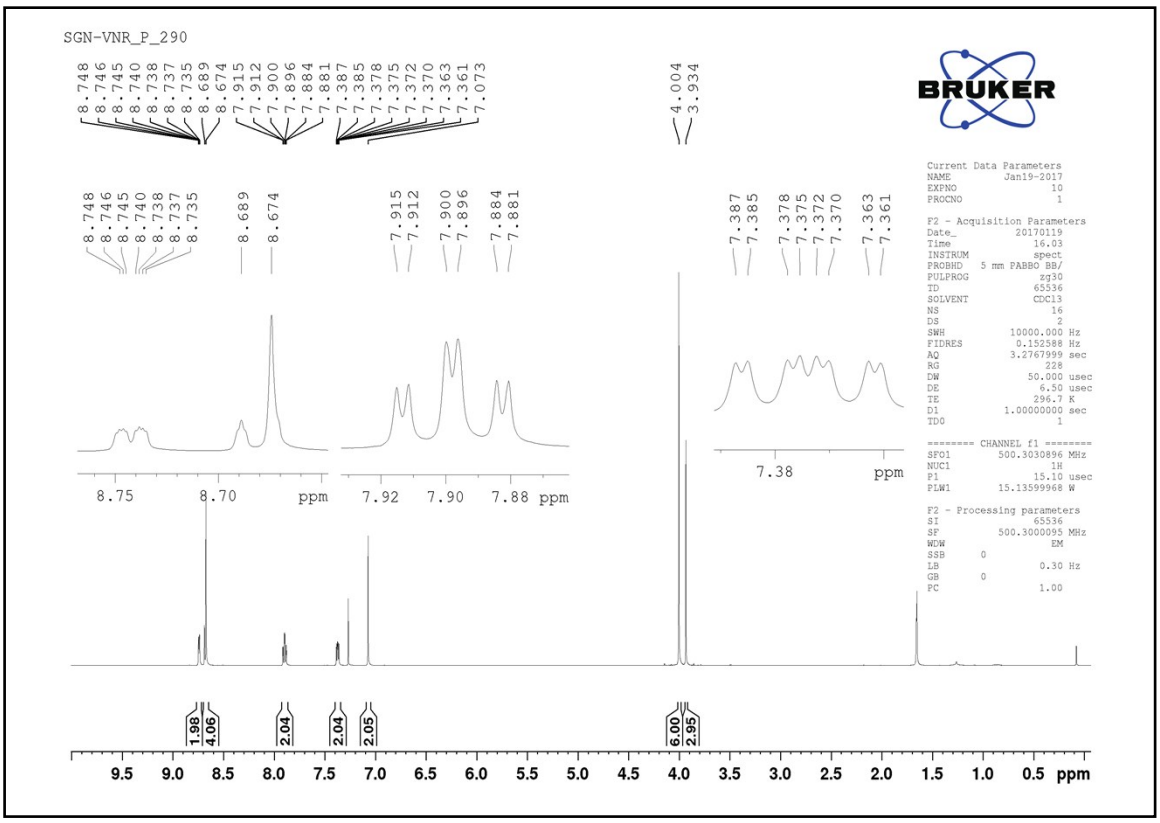

Figure S9. ^{1}H NMR spectrum of ligand **L** in $CDCl_3$.

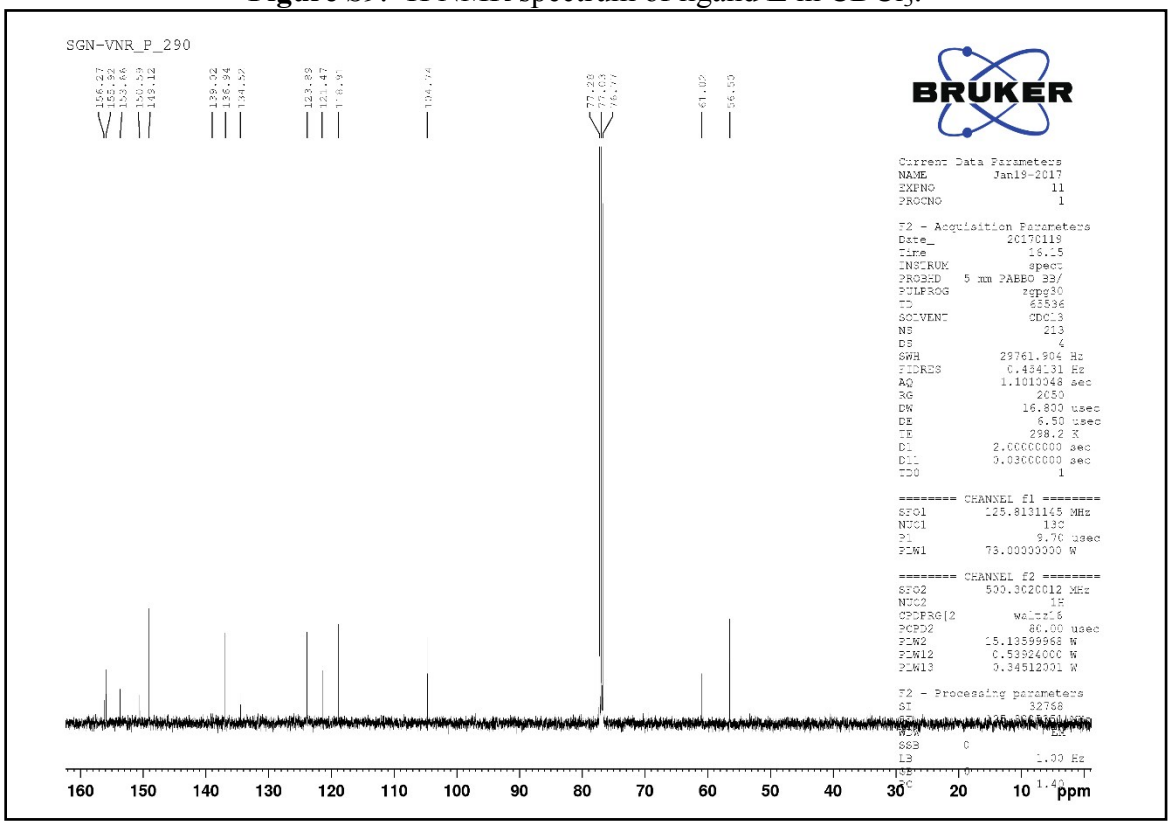

Figure S10. ^{13}C NMR spectrum of ligand **L** in $CDCl_3$.

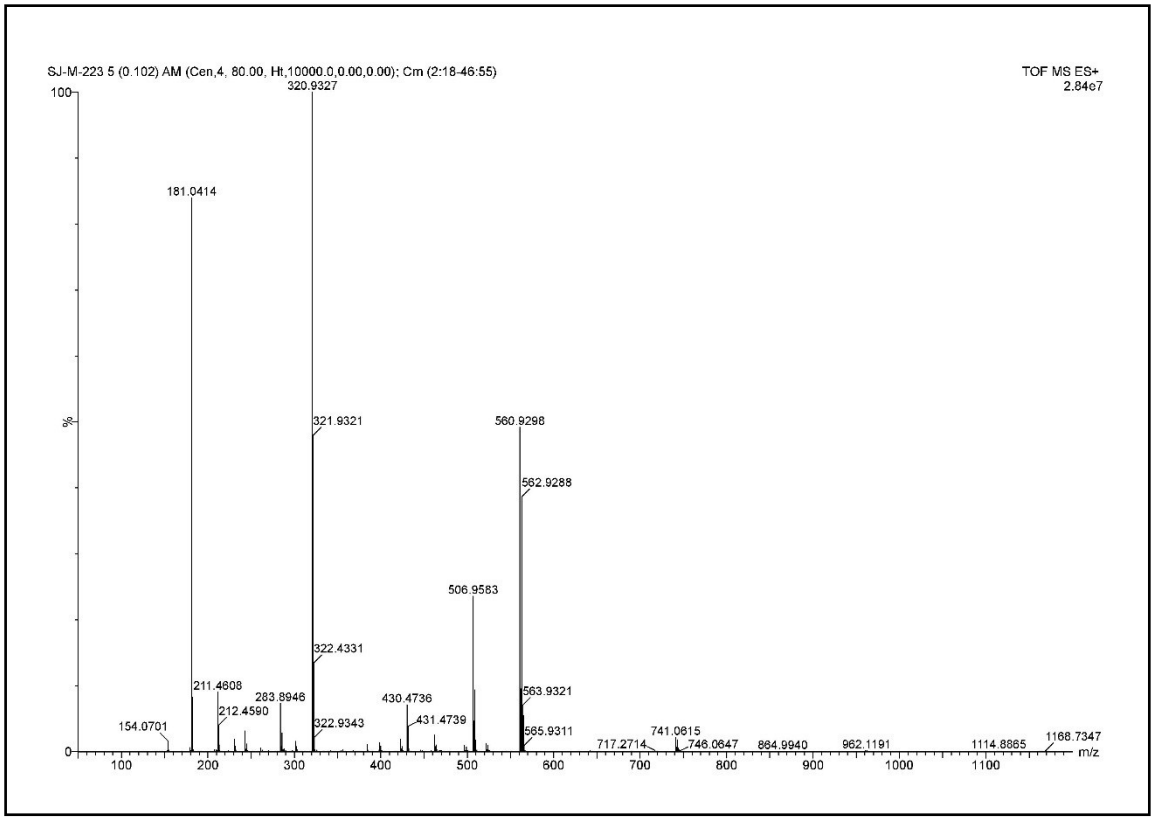

Figure S11. ESI-Mass spectrum of **C-I** recorded in MeCN.

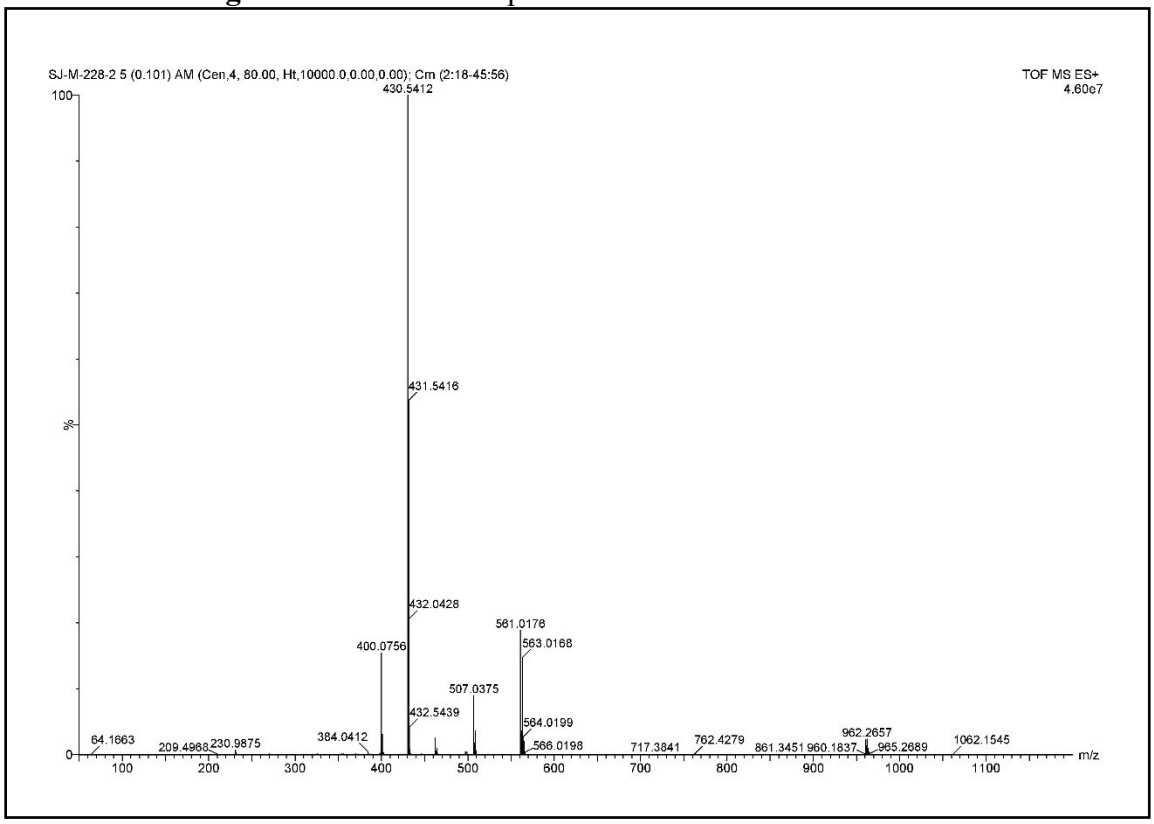

Figure S12. ESI-Mass spectrum of **C-II** recorded in MeCN.

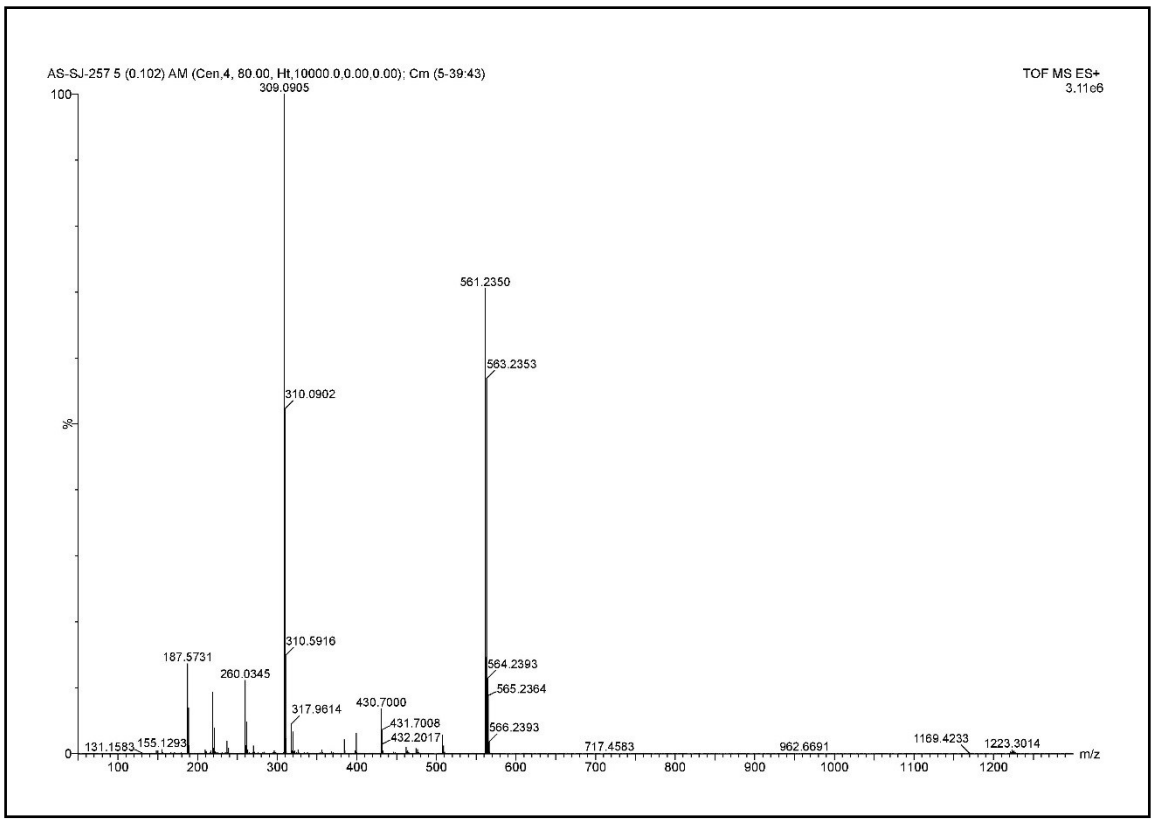

Figure S13. ESI-Mass spectrum of **C-III** recorded in MeCN.

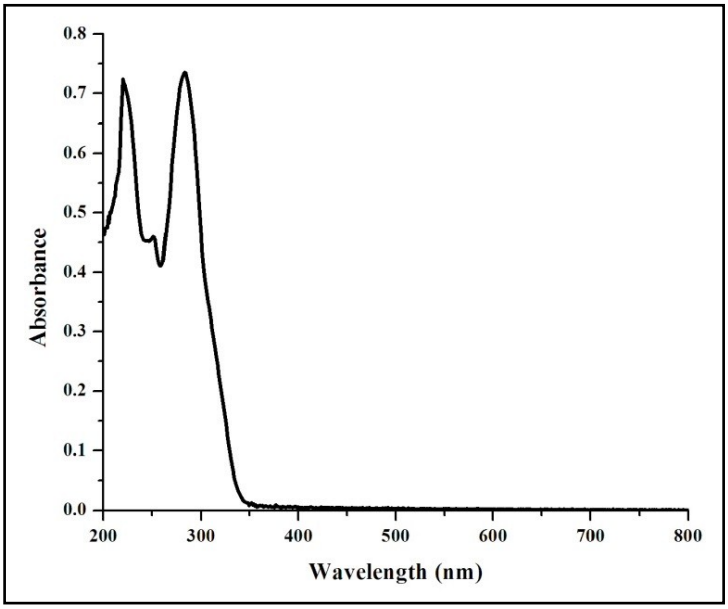

Figure S14. UV-Vis spectrum of **L** (20 μM) in MeCN

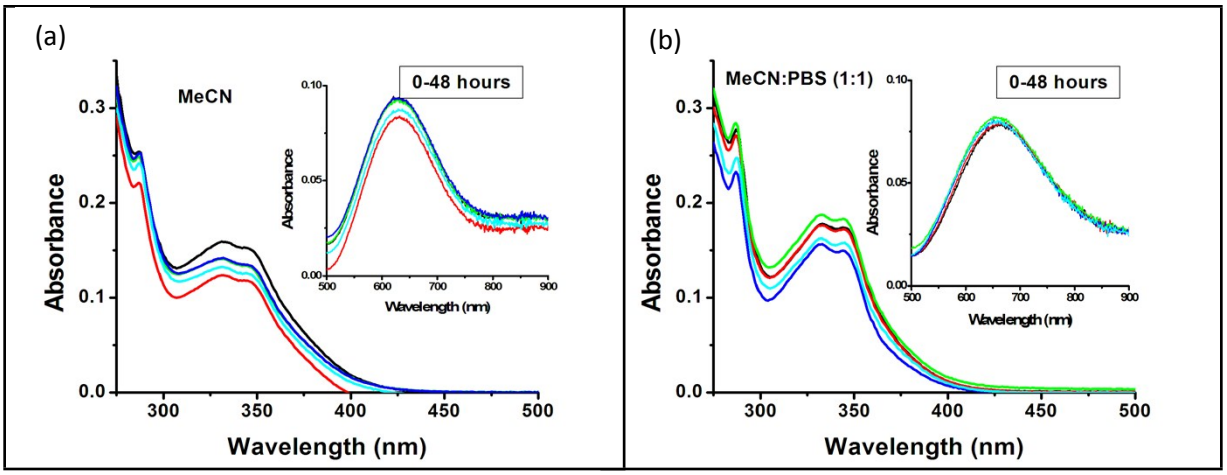

Figure S15. UV- Visible absorption spectra of **C-I** recorded in (a) MeCN and; (b) MeCN:PBS buffer (1:1) upto 48 h at 298 K.

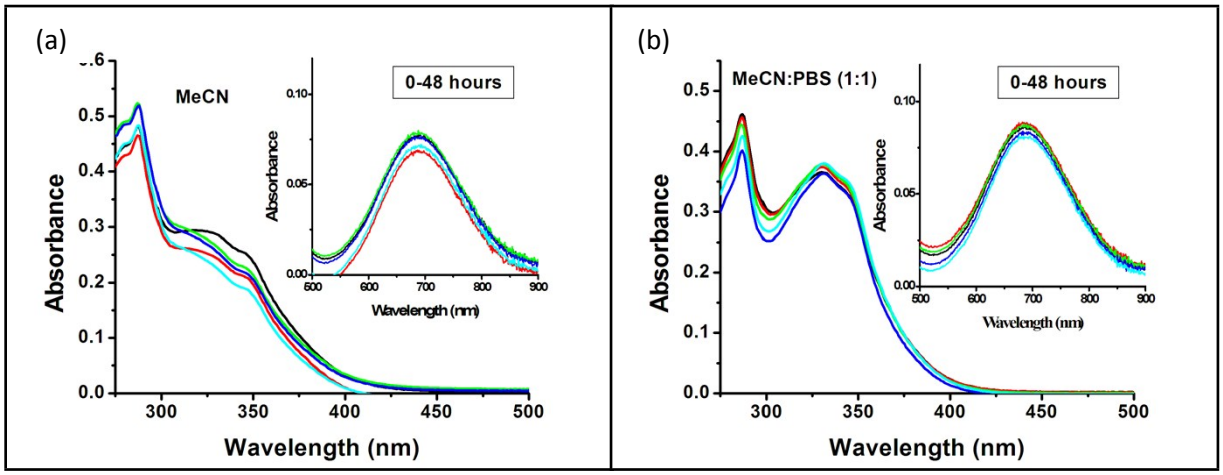

Figure S16. UV- Visible absorption spectra of **C-II** recorded in (a) MeCN and; (b) MeCN:PBS buffer (1:1) upto 48 h at 298 K.

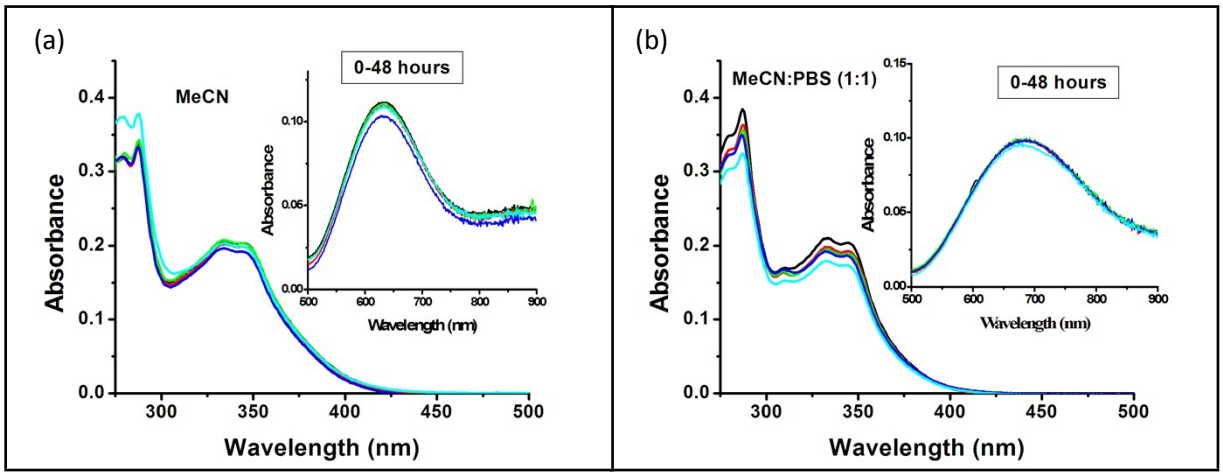

Figure S17. UV- Visible absorption spectra of **C-III** recorded in (a) MeCN and; (b) MeCN:PBS buffer (1:1) upto 48 h at 298 K

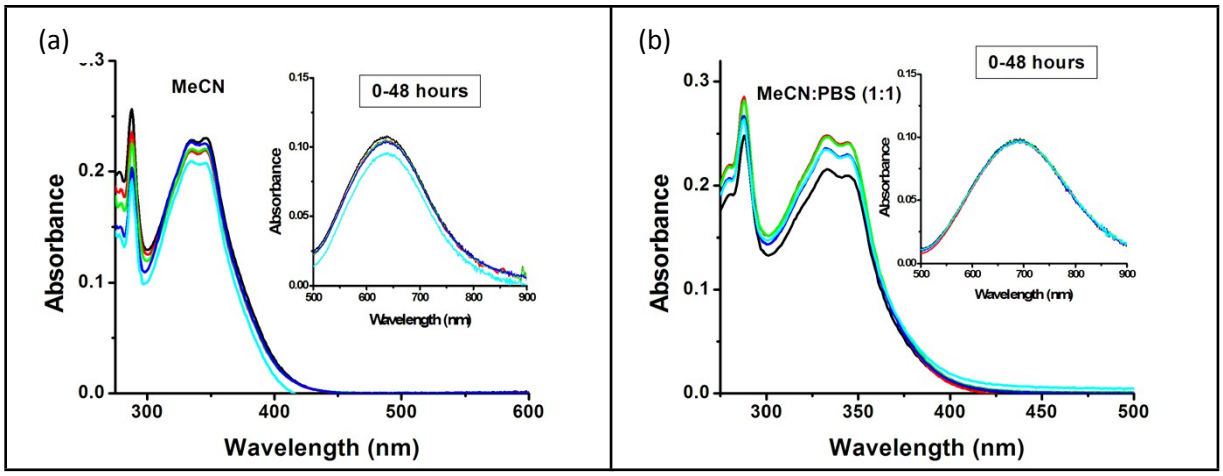

Figure S18. UV- Visible absorption spectra of **C-IV** recorded in (a) MeCN and; (b) MeCN:PBS buffer (1:1) upto 48 h at 298 K

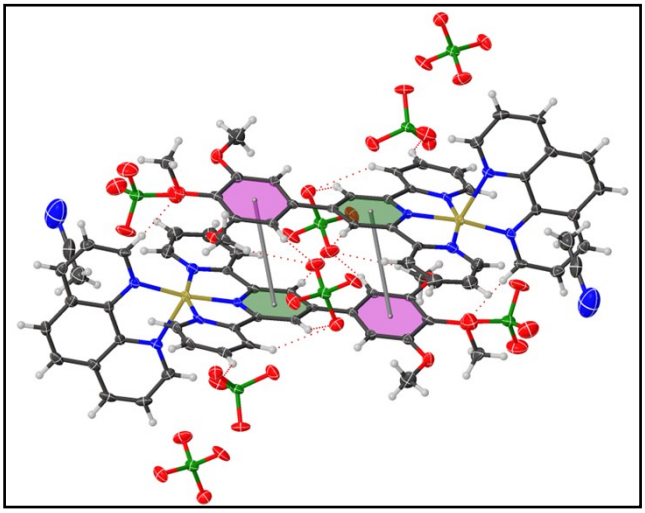

Figure S19. Crystal packing of **C-I** showing π-π interaction and H-bonding.

π-π interactions and hydrogen bond parameters (Å, °) for **C-I**

Cg(i)…Cg(j)	**Distance**	**Dihedral angle**	**Slippage**	**Symmetry**	
Cg(8)…Cg(9)	3.974(3)	14.00	1.857	1-x, 1-y, -z	
D-H…A	**D-H**	**A…H**	**D…A**	**<D-A…H**	**Symmetry**
C1-H1A…O4	0.9600	2.6000	3.531(10)	164.00	1-x,1-y,1-z
C4-H4…O4	0.9300	2.5200	3.422(8)	163.00	1-x,1-y,1-z
C11-H11…O4	0.9300	2.4800	3.408(7)	173.00	1-x,1-y,1-z
C19-H19…O7	0.9300	2.5800	3.384(8)	145.00	x,y,-1+z
C24-H24…O7	0.9300	2.4700	3.314(7)	150.00	x,y,-1+z
C26-H26…O6	0.9300	2.3400	3.149(8)	146.00	1-x,-1/2+y,1/2-z
C34-H34…O2	0.9300	2.5100	3.217(8)	133.0	1-x,1-y,-z
C36-H36…O9	0.9300	2.6000	3.393(9)	144.00	-x,1-y,-z

Cg(8): N5-C12-C24-C10-C11-C13; Cg(9): C2-C3-C4-C9-C8-C5

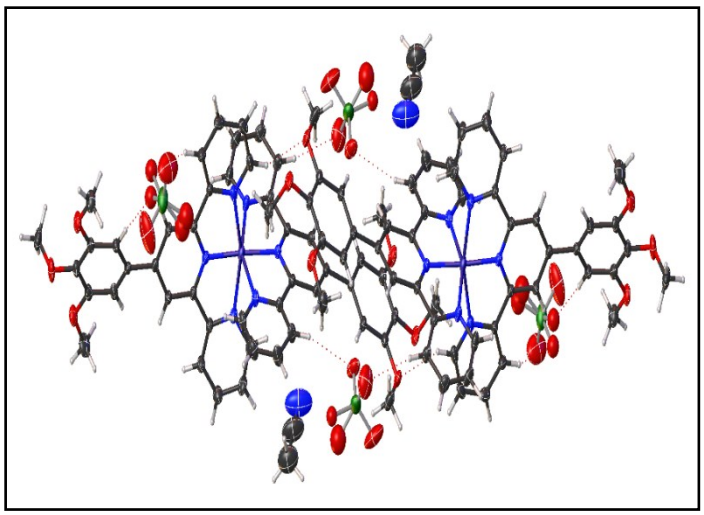

Figure S20. Crystal packing of **C-II** showing H-bonding.

Hydrogen bond parameters (Å, °) for **C-II**

D-H…A	D-H	A…H	D…A	<D-A…H	Symmetry
C2-H2A…O10	0.9600	2.3100	2.788(7)	110.00	
C3-H3A…O3	0.9600	2.5800	3.227(10)	125.00	x,y,1+z
C3-H3B…O11	0.9600	2.5500	3.492(7)	166.00	x,y,1+z
C016-H016…O5	0.9300	2.5500	3.366(10)	147.00	
C017-H017…O1	0.9300	2.5500	3.468(11)	171.00	1-x,1-y,1-z
C01B-H01B…O3	0.9300	2.5800	3.486(9)	166.00	x,y,1+z
C01E-H01E…O8	0.9300	2.4100	3.181(7)	140.0	1-x,1-y,2-z
C01N-H01N…O3	0.9300	2.4400	3.219(12)	141.00	2-x,2-y,1-z

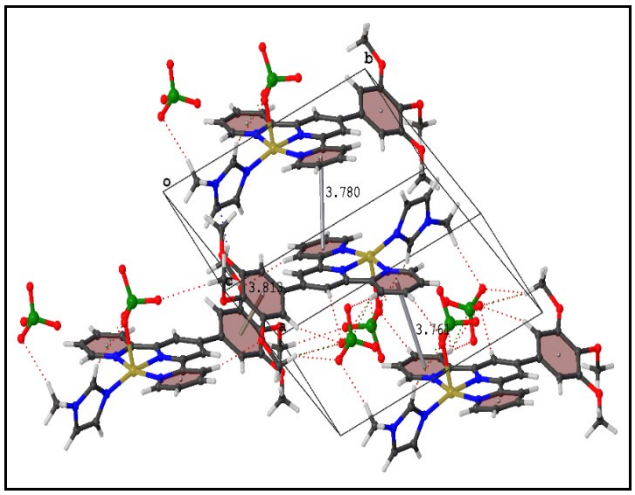

Figure S21. Crystal packing of **C-IV** showing π-π interaction and H-bonding.

π-π interactions and hydrogen bond parameters (Å, °) for **C-IV**

Cg(i)…Cg(j)	**Distance**	**Dihedral angle**	**Slippage**	**Symmetry**	
Cg(4)…Cg(4)	3.761(2)	0.00	1.844	2-x,1-y,1-z	
Cg(6)…Cg(6)	3.7803(18)	0.00	1.839	1-x,1-y,-z	
Cg(7)…Cg(7)	3.8130(19)	0.00	1.457	1-x,-y,1-z	
D-H…A	**D-H**	**A…H**	**D…A**	**<D-A…H**	**Symmetry**
C7-H7…O11	0.9300	2.5900	3.427(6)	150.00	2-x,1-y,1-z
C14-H14…O3	0.9300	2.5900	3.517(4)	172.00	-1+x,y,z
C21-H21…O4	0.9300	2.3800	3.093(4)	133.00	2-x,1-y,-z
C24-H24A…O7	0.9600	2.4400	3.223(6)	139.00	-x,-y,1-z
C25-H25…O4	0.9300	2.4500	3.285(5)	149.00	
C28-H28B…O9	0.9600	2.5700	3.482(6)	160.00	
C28-H28C…O2	0.9600	2.4700	3.425(5)	173.0	2-x,1-y,-z

Cg(4): N1-C1-C2-C3-C4-C5; Cg(6): N3-C17-C18-C19-C20-C21; Cg(7): C9-C10-C11-C12-C13-C14

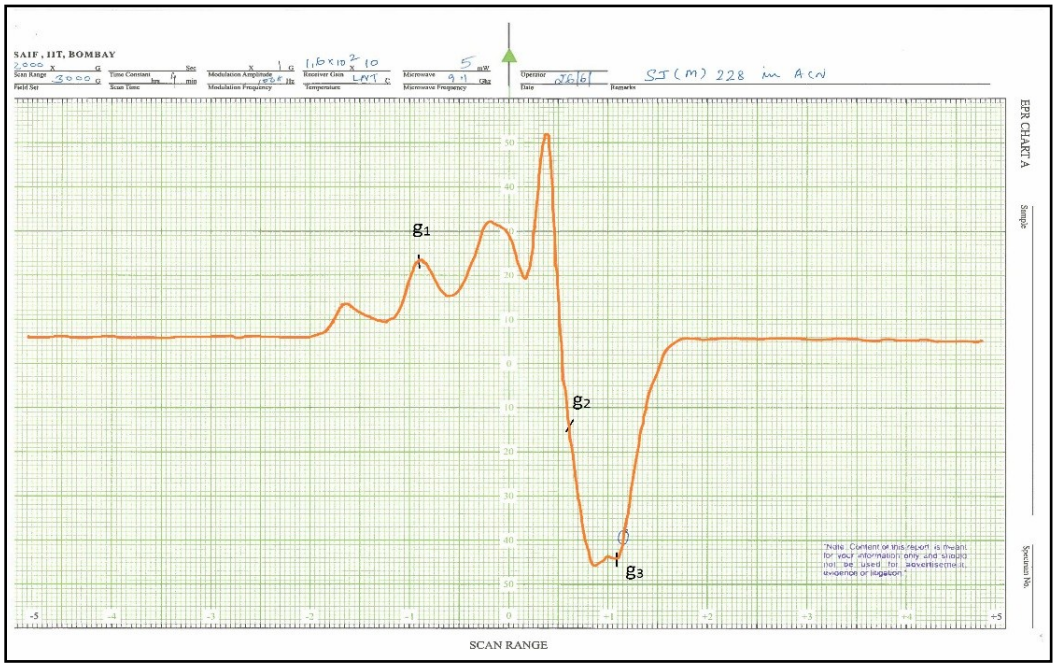

Figure S22. X-band EPR spectrum of complex **C-II** in MeCN glass at 77 K (frequency 9.1 GHz and 100 kHz field).

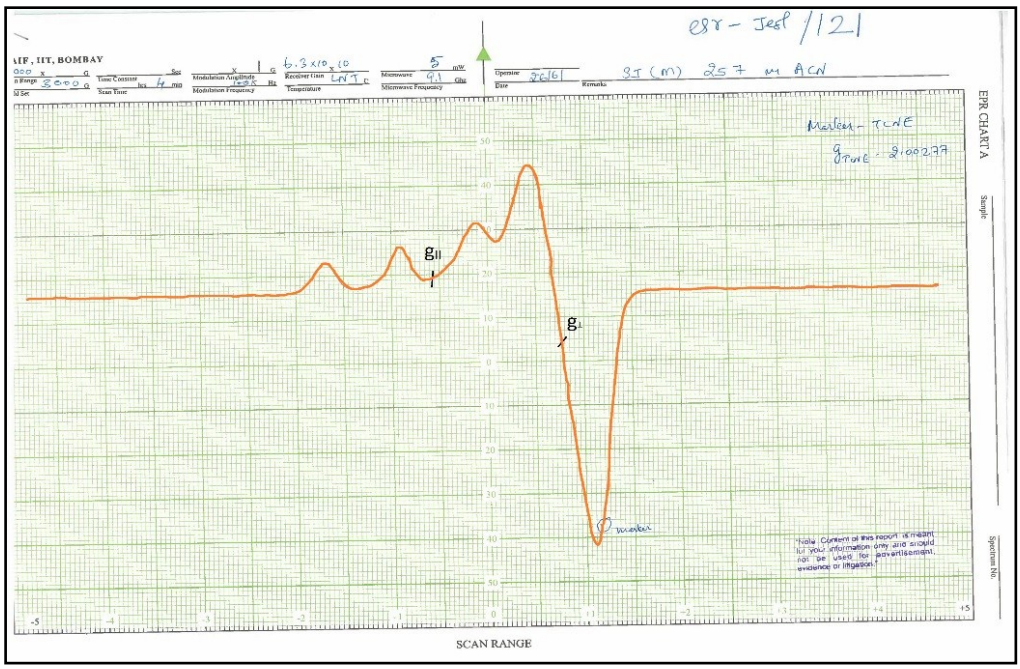

Figure S23. X-band EPR spectrum of complex **C-III** in MeCN glass at 77 K (frequency 9.1 GHz and 100 kHz field).

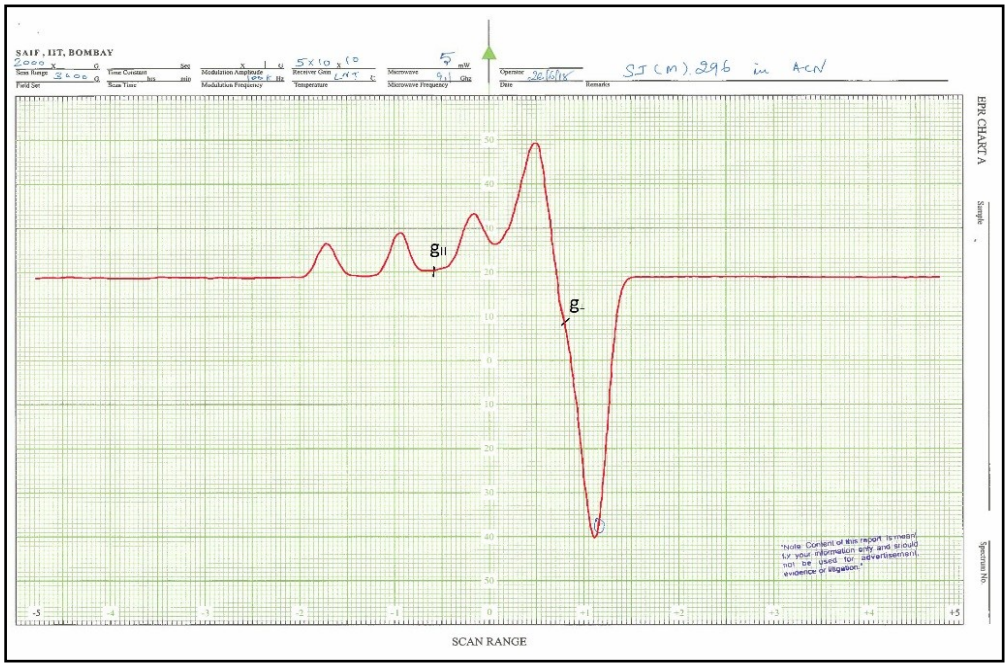

Figure S24. X-band EPR spectrum of complex **C-IV** in MeCN glass at 77 K (frequency 9.1 GHz and 100 kHz field).

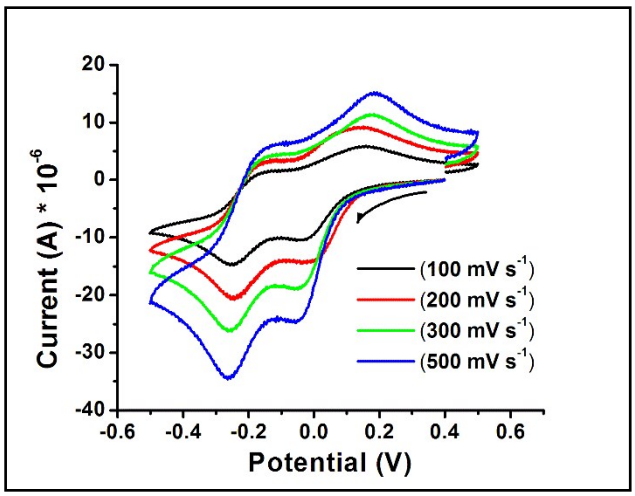

Figure S25. Cyclic voltammogram of **C-I** (1 mM) solution in dry CH_3CN and 0.1 M TBAP as supporting electrolyte *vs.* Ag wire at varying scan rates.

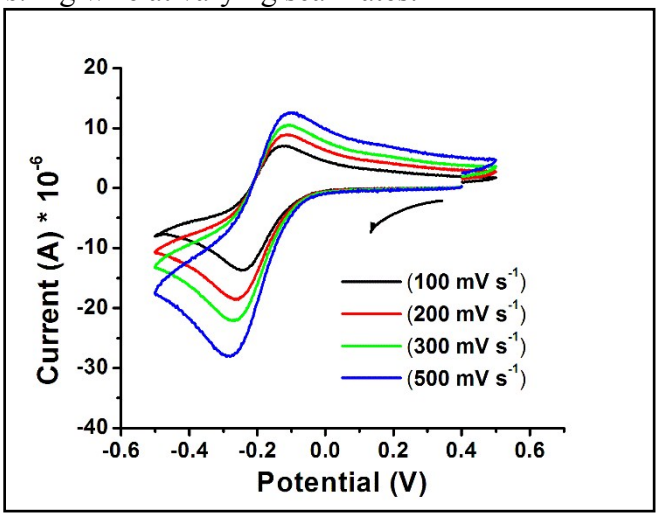

Figure S26. Cyclic voltammogram of **C-II** (1 mM) solution in dry CH_3CN and 0.1 M TBAP as supporting electrolyte *vs.* Ag wire at varying scan rates.

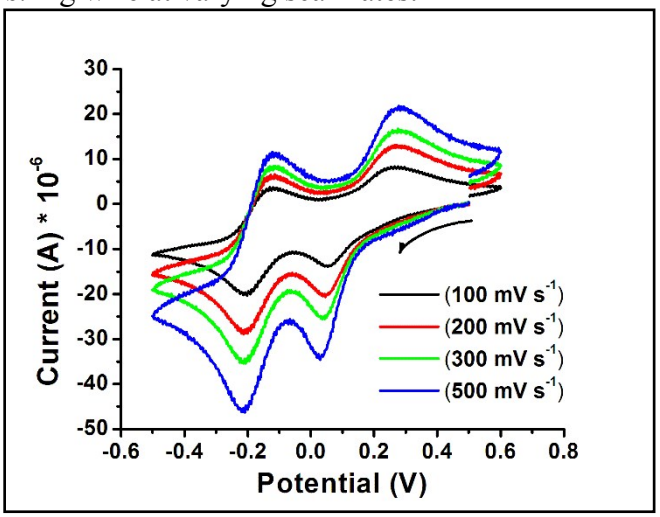

Figure S27. Cyclic voltammogram of **C-III** (1 mM) solution in dry CH_3CN and 0.1 M TBAP as supporting electrolyte *vs.* Ag wire at varying scan rates.

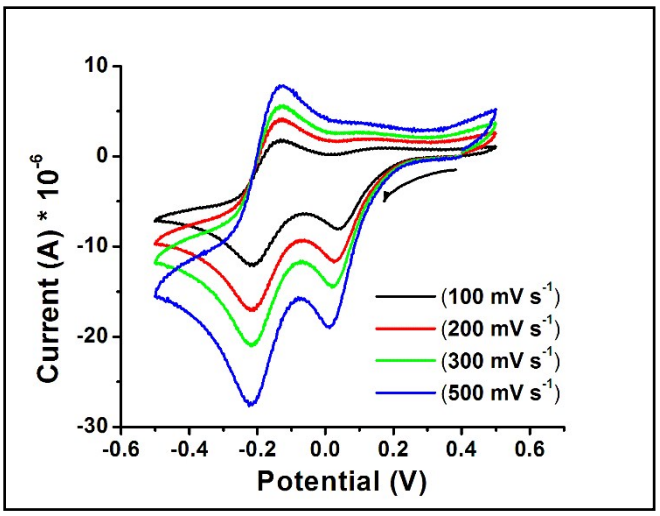

Figure S28. Cyclic voltammogram of **C-IV** (1 mM) solution in dry CH_3CN and 0.1 M TBAP as supporting electrolyte *vs.* Ag wire at varying scan rates.

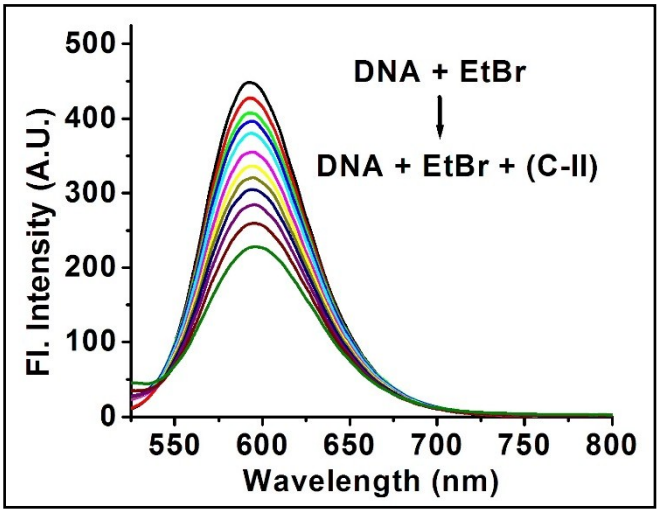

Figure S29. Plot of fluorescence emission intensity I versus wavelength λ for DNA-EtBr at different concentrations of **C-II**. The arrow shows the change in intensity of emission on increasing amount of the complex from 0 to 50 μM.

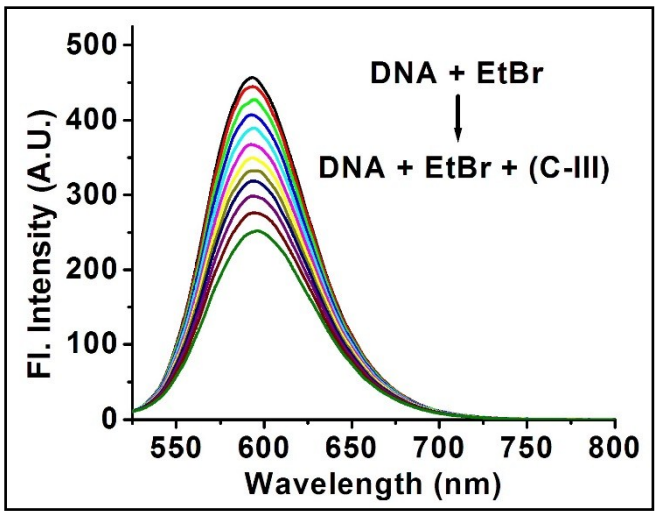

Figure S30. Plot of fluorescence emission intensity *I* versus wavelength λ for DNA-EtBr at different concentrations of **C-III**. The arrow shows the change in intensity of emission on increasing amount of the complex from 0 to 50 μM.

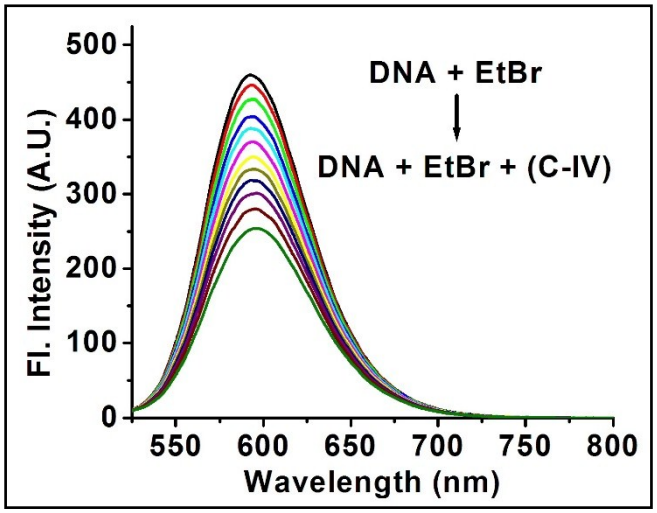

Figure S31. Plot of fluorescence emission intensity *I* versus wavelength λ for DNA-EtBr at different concentrations of **C-IV**. The arrow shows the change in intensity of emission on increasing amount of the complex from 0 to 50 μM.

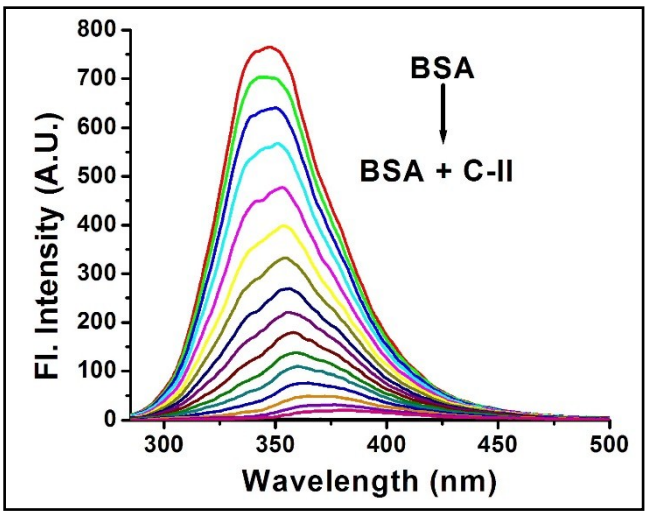

Figure S32. Plot of fluorescence emission intensity *I* versus wavelength λ for BSA at different concentrations of **C-II**. The arrow shows the change in intensity of emission on increasing amount of the complex from 0 to around 50 μM.

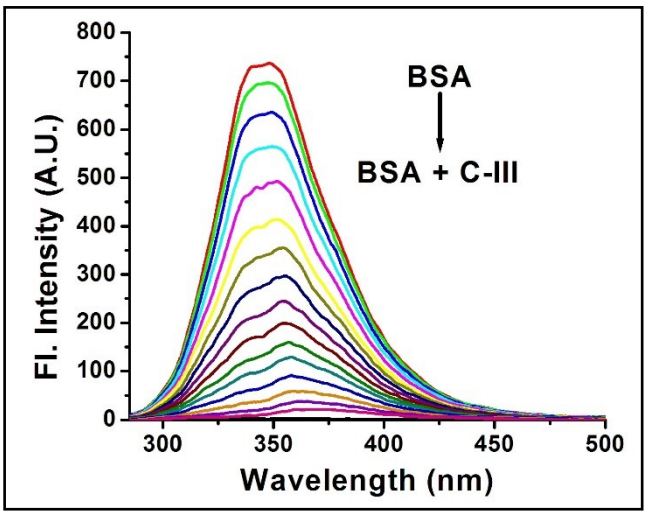

Figure S33. Plot of fluorescence emission intensity *I* versus wavelength λ for BSA at different concentrations of **C-III**. The arrow shows the change in intensity of emission on increasing amount of the complex from 0 to around 50 μM.

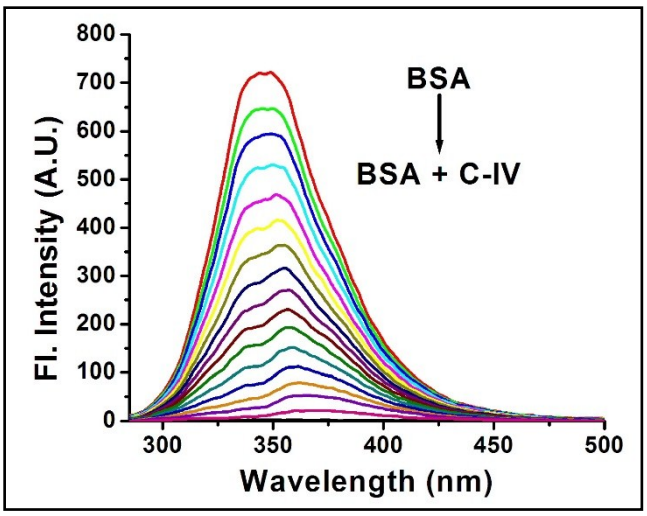

Figure S34. Plot of fluorescence emission intensity I versus wavelength λ for BSA at different concentrations of **C-IV**. The arrow shows the change in intensity of emission on increasing amount of the complex from 0 to around 50 μM.

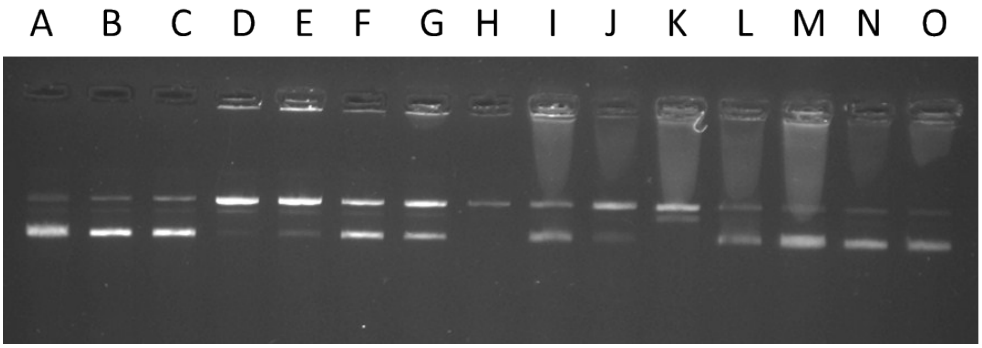

Figure S35. Agarose gel electrophoresis for complexes **C-I** to **C-IV** showing DNA aggregation in presence of H_2O_2. Lane A: DNA only; Lane B: Buffer control; Lane C: H_2O_2 (500 μM) control; Lane D: **C-I** (500 μM) control; Lane E: **C-II** (500 μM) control; Lane F: **C-III** (500 μM) control; Lane G: **C-IV** (500 μM) control; Lane H: **C-I** (100 μM) + H_2O_2 (500 μM); Lane I: **C-II** (100 μM) + H_2O_2 (500 μM); Lane J: **C-III** (100 μM) + H_2O_2 (500 μM); Lane K: **C-IV** (100 μM) + H_2O_2 (500 μM); Lane L: **C-I** (500 μM) + H_2O_2 (500 μM); Lane M: **C-II** (500 μM) + H_2O_2 (500 μM); Lane N: **C-III** (500 μM) + H_2O_2 (500 μM); Lane O: **C-IV** (500 μM) + H_2O_2 (500 μM)

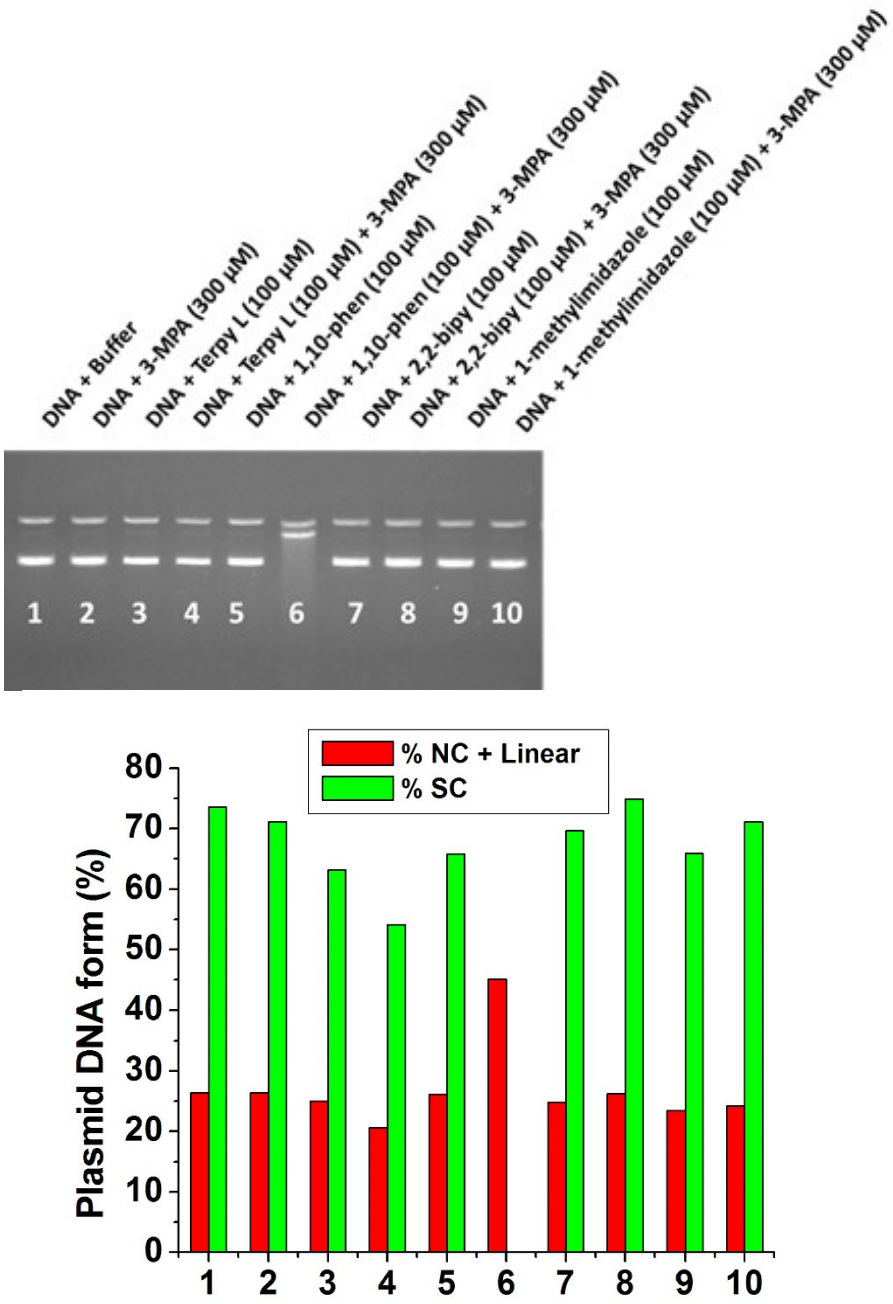

Figure S36. (Top): Agarose gel electrophoresis for terpyridine ligand (**L**) and co-ligands (1,10-phenanthroline, 2,2'-bipyridine, 3-methylimidazole in absence and presence of 3-MPA; (Bottom): % Plasmid DNA form present in each lane.

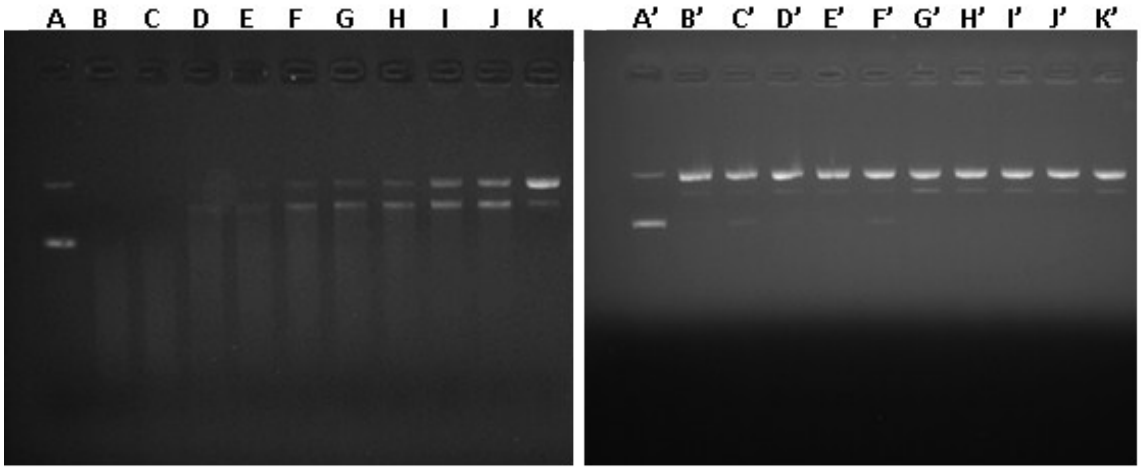

Figure S37 (Left): Gel electrophoresis diagram showing chemical nuclease activity of **C-I** to **C-IV** in the presence of various controls. Lane A: Buffer control; Lane B: DNA + **C-I** (100 μM) + MPA (500 μM); Lane C: DNA + **C-I** (100 μM) + MPA (500 μM) + D_2O (2.5 mM); Lane D: DNA + **C-I** (100 μM) + MPA (500 μM)+ DMSO (2.5 mM); Lane E: DNA + **C-I** (100 μM) + MPA (500 μM)+ NaN_3 (2.5 mM); Lane F: DNA + **C-I** (100 μM) + MPA (500 μM) + KI (2.5 mM); Lane G: DNA + **C-II** (100 μM) + MPA (500 μM); Lane H: DNA + **C-II** (100 μM) + MPA (500 μM)+ D_2O (2.5 mM); Lane I: DNA + **C-II** (100 μM)+ MPA (500 μM)+ DMSO (2.5 mM); Lane J: DNA + **C-II** (100 μM)+ MPA (500 μM)+ NaN_3 (2.5 mM); Lane K: DNA + **C-II** (100 μM) + MPA (500 μM)+ KI (2.5 mM).

(Right): Lane A': Buffer control; Lane B': DNA + **C-III** (100 μM) + MPA (500 μM); Lane C': DNA + **C-III** (100 μM) + MPA (500 μM)+ D_2O (2.5 mM); Lane D': DNA + **C-III** (100 μM) + MPA (500 μM)+ DMSO (2.5 mM); Lane E': DNA + **C-III** (100 μM) + MPA (500 μM)+ NaN_3 (2.5 mM); Lane F': DNA + **C-III** (100 μM) + MPA (500 μM)+ KI (2.5 mM); Lane G': DNA + **C-IV** (100 μM) + MPA (500 μM); Lane H': DNA + **C-IV** (100 μM) + MPA (500 μM)+ D_2O (2.5 mM); Lane I': DNA + **C-IV** (100 μM) + MPA (500 μM)+ DMSO (2.5 mM); Lane J': DNA + **C-IV** (100 μM) + MPA (500 μM)+ NaN_3 (2.5 mM); Lane K': DNA + **C-IV** (100 μM) + MPA (500 μM)+ KI (2.5 mM).

Table S1. Consolidated characterization data for copper(II) complexes (**C-I - C-IV**).

Complex	**FTIR, cm^{-1} (KBr disc)**	**λ_{max}, nm (ε, $M^{-1}cm^{-1}$) (in MeCN)**	**ESI-MS *m/z* found (calculated): [(M^{2+}–$2ClO_4$)/2] in MeCN**	**CHN found (calculated)**	**Conductance ($S.cm^{-1}M^{-1}$)**
C-I	3000 (w), 1600 (m), 1404 (m), 1085 (vs), 622 (m)	223 (7.5 x 10^4); 270 (5.1 x 10^4); 330 (1.9 x 10^4); 690 (1.2 x 10^2)	320.933 (321.080)	C=51.87 (51.35); H=3.68 (3.47); N=8.03 (8.32)	310
C-II	2945 (w),	222 (8.4 x	430.541	C=54.69 (54.32);	280

	1610 (m), 1480 (m), 1090 (vs), 620 (m)	10^4); 265 (4.0 x 10^4); 287 (3.8 x 10^4); 332 (3.9 x 10^4); 689 (8.7 x 10^1)	(430.625)	H=4.09 (3.99); N=7.22 (7.72)	
C-III.H_2O	3520 (w), 3070 (w), 1605 (m), 1405 (m), 1090 (vs), 625 (m)	222 (6.3 x 10^4); 288 (3.3 x 10^4); 340 (2.0 x 10^4); 637 (1.1 x 10^2)	309.0905 (309.080)	C=48.54 (48.84); H=3.42 (3.74); N=8.72 (8.38)	350
C-IV	2935 (w), 1605 (m), 1405 (m), 1100 (vs), 620 (m)	222 (5.7 x 10^4); 288 (2.0 x 10^4); 340 (1.9 x 10^4); 640 (1.1 x 10^2)	----	C=45.02 (45.20); H=3.59 (3.66); N=9.89 (9.41)	320

Table S2: Summary of crystal data for complexes **C-I**, **C-II** and **C-IV**

Compound	**C-I**	**C-II**	**C-IV**
Formula	$C_{76}H_{64}Cl_4Cu_2N_{12}O_{22}$	$C_{50}H_{45}Cl_2CuN_7O_{14}$	$C_{28}H_{27}Cl_2CuN_5O_{11}$
Formula weight/ g.mol^{-1}	1766.27	1102.36	743.98
T (K)	296(2)	296(2)	293(2)
Crystal system	Monoclinic	Triclinic	Triclinic
Space group	$P2_1/c$	$P\bar{1}$	$P\bar{1}$
a/Å	19.078(5)	9.6483(4)	9.1079(4)
b/Å	12.031(3)	12.9618(6)	12.5746(4)
c/Å	17.935(4)	20.9170(9)	14.8504(7)
α/°	90	91.460(3)	70.650(4)
β/°	113.406(12)	100.086(3)	88.016(4)
γ/°	90	107.065(3)	73.255(4)
V/Å^3	3778.0(16)	2453.82(19)	1533.18(12)
Z	2	2	2
ρ_{calcd} (mg/m^3)	1.553	1.436	1.612
Absorption coefficient (μ) (mm^{-1})	0.791	0.627	0.956
F (000)	1812	1094	762
R (int)	0.2052	0.0223	0.0198
Data/restraints/parameters	6633 / 0 / 527	8613 / 0 / 674	5385 / 0 / 424
Goodness-of-fit on F^2	1.117	1.169	1.057
Final R indices [I>2σ(I)] (R_1,wR_2)	0.0825, 0.2189	0.0768, 0.1962	0.0427, 0.1152
R indices (all data) (R_1, wR_2)	0.0989, 0.2326	0.0860, 0.2029	0.0486, 0.1208
Largest diff. peak and hole	0.917 and -1.087	1.386 and -0.578	0.911 and -0.518

(e.Å^{-3})			

Table S3. Selected bond lengths (Å) and bond angles (°) for complexes **C-I**, **C-II** and **C-IV**

C-I					
Selected bonds		Selected angles			
Cu(1)-N(5)	1.944(4)	N(5)-Cu(1)-N(1)	170.58(19)	N(4)-Cu(1)-N(3)	158.5(2)
Cu(1)-N(1)	2.000(5)	N(5)-Cu(1)-N(4)	79.48(19)	N(5)-Cu(1)-N(2)	109.36(18)
Cu(1)-N(4)	2.044(5)	N(1)-Cu(1)-N(4)	100.5(2)	N(1)-Cu(1)-N(2)	79.98(19)
Cu(1)-N(3)	2.045(5)	N(5)-Cu(1)-N(3)	80.61(19)	N(4)-Cu(1)-N(2)	99.88(19)
Cu(1)-N(2)	2.215(5)	N(1)-Cu(1)-N(3)	97.77(19)	N(3)-Cu(1)-N(2)	94.38(18)
C-II					
Selected bonds		Selected angles			
Cu(01)-N(2)	1.947(4)	N(2)-Cu(01)-N(5)	176.74(16)	N(2)-Cu(01)-N(6)	103.24(16)
Cu(01)-N(5)	1.998(4)	N(2)-Cu(01)-N(3)	78.62(16)	N(5)-Cu(01)-N(6)	76.49(15)
Cu(01)-N(3)	2.109(5)	N(5)-Cu(01)-N(3)	104.63(16)	N(3)-Cu(01)-N(6)	94.14(17)
Cu(01)-N(1)	2.112(4)	N(2)-Cu(01)-N(1)	78.64(16)	N(1)-Cu(01)-N(6)	89.75(17)
Cu(01)-N(6)	2.223(4)	N(5)-Cu(01)-N(1)	98.11(16)	N(2)-Cu(01)-N(4)	103.42(16)
Cu(01)-N(4)	2.240(4)	N(3)-Cu(01)-N(1)	157.22(16)	N(5)-Cu(01)-N(4)	76.97(15)
		N(3)-Cu(01)-N(4)	89.75(17)	N(1)-Cu(01)-N(4)	96.80(17)
		N(6)-Cu(01)-N(4)	153.30(15)		
C-IV					
Selected bonds		Selected angles			
Cu(01)-N(2)	1.923(2)	N(2)-Cu(01)-N(4)	167.10(11)	N(3)-Cu(01)-N(1)	159.88(10)
Cu(01)-N(4)	1.950(2)	N(2)-Cu(01)-N(3)	80.20(9)	N(2)-Cu(01)-O(1)	95.26(10)
Cu(01)-N(3)	2.025(2)	N(4)-Cu(01)-N(3)	101.98(10)	N(4)-Cu(01)-O(1)	97.25(10)
Cu(01)-N(1)	2.035(3)	N(2)-Cu(01)-N(1)	79.75(10)	N(3)-Cu(01)-O(1)	94.06(9)
Cu(01)-O(1)	2.389(2)	N(4)-Cu(01)-N(1)	97.94(11)	N(1)-Cu(01)-O(1)	86.17(9)

Table S4. Summary of IC_{50} values for similar Cu(II) complexes in cancer cell line.

Complex	**IC_{50} (μM)**	**Ref.**
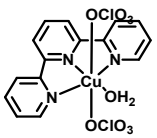 [Cu(terpy)(ClO$_4$)$_2$(H$_2$O)] (1) 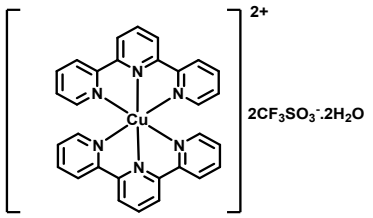 [Cu(terpy)$_2$](CF$_3$SO$_3$)$_2$.2H$_2$O (2)	(1) 1.9 ± 0.1[a] (2) 1.2 ± 0.1[a]	1

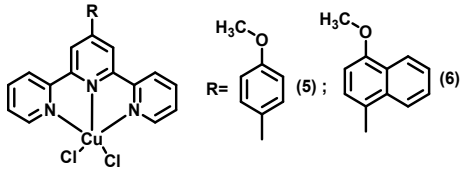				(5) 1.02 ± 0.04[b] 2.54 ± 0.05[c] (6) 0.40 ± 0.06 [b] 0.95 ±0.05 [c]	2
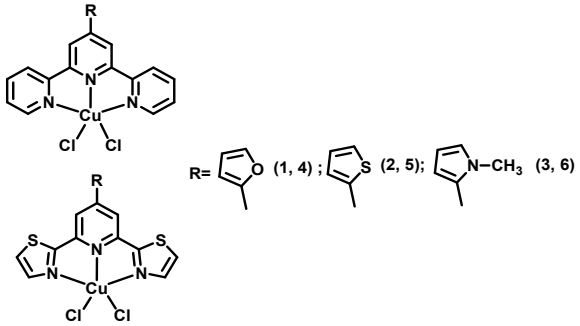					3
(1)	17.3± 0.3[b]	20.5± 0.2[a]	43± 0.3[d]	2.9± 0.1[c]	
(2)	2.1± 0.1 [b]	4.2± 0.2[a]	>100[d]	>100[c]	
(3)	>100[b]	>100[a]	>100[d]	>100[c]	
(4)	81.7± 0.3[b]	64.3± 0.3[a]	>100[d]	5.9± 0.1[c]	
(5)	20.5± 0.4[b]	22.6± 0.3[a]	62.3± 0.5[d]	4.6± 0.1[c]	
(6)	>100[b]	70.1± 0.4[a]	89± 0.5[d]	2.6± 0.1[c]	
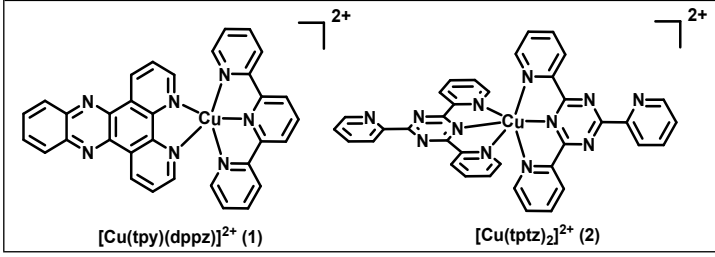				(1) 4.57 μM [d] (2) 1.98 μM [d]	4

[Cu(tpy)(dppz)]$^{2+}$ (1) [Cu(tptz$_2$)]$^{2+}$ (2)

[a] A549 cell; [b] HCT116 cell; [c]A2780 cell; [d]MCF-7 cell

1. B. Đ. Glišić, J. Nikodinovic-Runic, T. Ilic-Tomic, H. Wadepohl, A. Veselinović, I. M. Opsenica and M. I. Djuran, *Polyhedron*, 2018, **139**, 313-322.
2. A. Maroń, K. Czerwińska, B. Machura, L. Raposo, C. Roma-Rodrigues, A. R. Fernandes, J. G. Małecki, A. Szlapa-Kula, S. Kula and S. Krompiec, *Dalton Trans.*, 2018, **47**, 6444-6463.
3. K. Czerwińska, B. Machura, S. Kula, S. Krompiec, K. Erfurt, C. Roma-Rodrigues, A. R. Fernandes, L. S. Shul'pina, N. S. Ikonnikov and G. B. Shul'pin, *Dalton Trans.*, 2017, **46**, 9591-9604.
4. M. Salimi, K. Abdi, H. M. Kandelous, H. Hadadzadeh, K. Azadmanesh, A. Amanzadeh and H. Sanati, *BioMetals*, 2015, **28**, 267-278.